RESEARCH ARTICLE

Effect of Alternated Multiaxial Stress State on Fatigue Strength and Relaxation of Residual Stress in Welded S355 Steel with Nonlinear and Combined Hardening

H. Khatib* and A. El Kebch

ISPS2I Laboratory, ENSAM Casablanca, University Hassan II, Casablanca 20000, Morocco

ABSTRACT - This work aims to analyse the effect of the alternated multiaxial stress state on the relaxation mechanisms of residual stresses and the integrity of welded S355 steel, presenting a nonlinear and combined hardening behaviour. The first part of this work proposes a model to predict the residual stresses introduced by the thermal effect of the welding process. The stresses resulting from the thermal cycle were integrated into a second model in which the material was subjected to a cyclic load to analyse the relaxation process. To ensure a good accuracy of the relaxation results, the kinematic and isotropic hardening were combined in a nonlinear model. In the last part of this paper, a multiaxial fatigue strength analysis was carried out, taking into account the effect of residual stresses and the relaxation process. The results show a considerable relaxation of the residual stresses if they are subjected to low load levels applied under specific conditions. The relaxed residual stresses can have a considerable effect on fatigue strength. Also, the importance of the consideration of the relaxation process on the accuracy of the fatigue strength results is illustrated.

1.0   INTRODUCTION

Several steel structures are subjected to an internal stress state in the absence of any external loads. These stresses can affect positively or negatively the integrity of these structures after the application of the external loads. At the microscopic scale, these stresses can be introduced by point or dislocation defects [1]-[3]. Other causes can also lead to a residual stress state, such as the anisotropy at the level of the metallic grains, which can produce a plastic strain heterogeneity between different grains [4]. These stresses can appear at the macroscopic level after localised plastic deformations on specific zones introduced by shaping processes or material removal [5]-[7]. In automotive structures, spot welds and bolted connections are an important source of residual stresses [8], [9].

In the case of butt welded connections, the intensity of the residual stresses is significant, and it approaches the yield limit [10]-[12], which justifies the effect of these stresses on the damage mechanism and crack propagation. Moreover, the state of these stresses is unstable during the mechanical load application [13],[14], which complicates the consideration of these stresses during the mechanical design process. Considering that these stresses are stable generates a significant difference between the calculated and experimental results. In order to analyse the impact of the external load on the residual stress relaxation and on fatigue strength, the paper is divided into three main parts, as in Figure 1.

The objective of the first part is to predict the residual stress state produced by the welding process. This result is obtained by building a numerical model simulating the motion of the heat source and the thermal strain produced by the thermal cycle. Based on this result, it is possible to obtain the residual stress field produced at the end of the welding process. The aim of the second part is to model the impact of the external loads on the stability of residual stresses. This is to visualise the instability of these stresses in several load cases. Thus, it is possible to classify loads according to their impact on the state of the residual stresses. In the third part of this paper, the objective is to analyse the effect of the external loads on the fatigue life of the weld joint, taking into account two main elements. First, the relaxation process under cyclic load, and second, the effect of the local triaxial stress state, applied after relaxation, on fatigue strength. These results can help engineers and designers to predict the stability and effects of eternal load on residual stresses on assembled parts; also, the obtained results could estimate the fluctuation of residual stresses according to the magnitude of the external load. These results evaluate more precisely the impact of the external load on the integrity of the designed structures by taking into account the instability of the residual stresses.

2.0   WELDING RESIDUAL STRESSES

2.1   Thermomechanical Modelling of Residual Stress

In the case of the welded assembly using arc welding, the residual stresses in the assembled parts are a consequence of the dimensional shrinkages after the application of a high temperature produced by the Joule effect. The high level of

---

temperature causes a variation of the mechanical properties, an evolution of the metallurgical structures, and a variation of the thermal proprieties. Due to the interaction between the different states (mechanical, metallurgical and thermal), the analysis of residual stresses is considered a coupled problem (as in Figure 2).

Step 1 : Residual stress modeling   Step 2 : Effect of the external load   Step 3 : Fatigue analysis
on the relaxation process

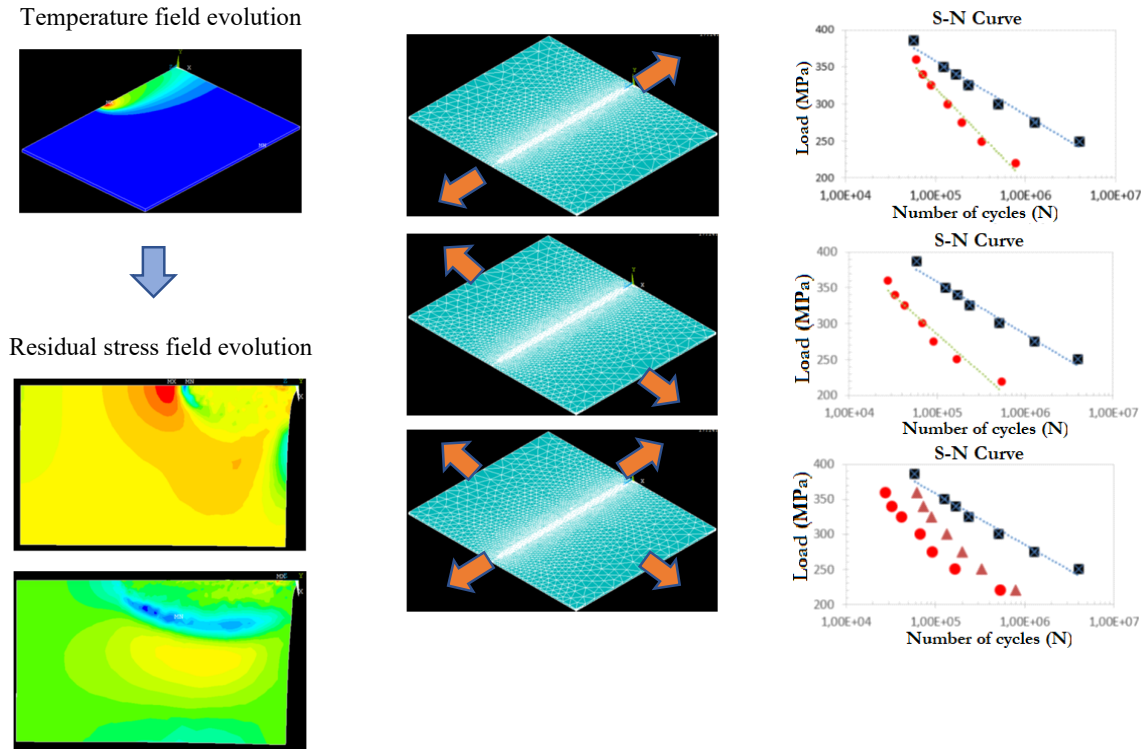Temperature field evolution

Residual stress field evolution

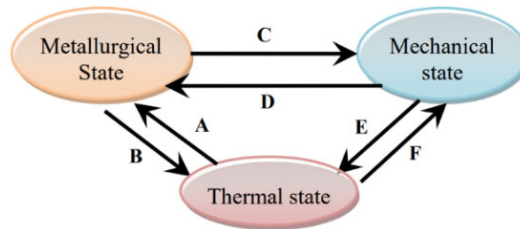Figure 1. Analysis approach adopted in this paper

Figure 2. Multiphysics interaction during welding

In our case, the finite element (FE) model developed for the estimation of the residual stresses is divided into two phases. Initially, the temperature field is evaluated considering the thermal properties as a function of the temperature which will require a step-by-step resolution. The second phase consists of evaluating the mechanical state (stress and strain), considering the direct impact of the temperature on each mechanical property such as Young's modulus and the yield limit. To model the temperature field evolution, it will be important to model the process of creation and transfer of heat toward the geometry of the material. In the case of arc welding, a significant quantity of this energy is absorbed by the material, which causes the fusion; an additional quantity will be lost by radiation or convection towards the surrounding area. To estimate the heat effectively absorbed by the material, we adopt an efficiency factor of 85%, according to [15].

The material considered for the analysis was the S355 structural steel with 5 mm thickness. The process operating parameters (current, voltage, and speed) applied in the model were examined at the laboratory to evaluate their adaptability to the material and the geometry. Due to the time required for the resolution and given the symmetry of the model, only half of the geometry in Figure 3(a) and 3(b) were considered during the resolution.
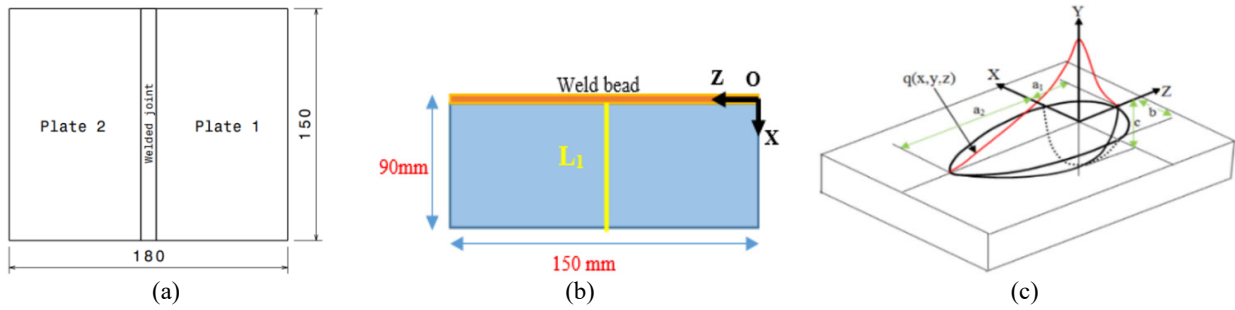
Figure 3. (a) Studied geometry, (b) analysed geometry and (c) geometry of the heat source (at welding current of 97 A, voltage between 27 V and 35 V, heat source speed of 3.33mm/s)

The heat produced by the electrical arc will be transferred to a volume (v) located on the weld bead in Figure 3(c) [16]. This volume is considered later as the heat source on the plate. The volume (v) has a double ellipsoidal geometry (Figure 3(c)). To estimate more accurately the evolution of the temperature field, the heat density (q) depends on the location of the point (X, Y, Z) where the heat density (q) is evaluated. The 'Z' axis was selected as the direction of the weld bead, and the'Y' axis is through the thickness. The heat density, q(X,Y,Z) is expressed as follows depending on the position of (X, Y, Z) [17]. This coordinate system is animated with the speed of the heat source of 3.33 mm/s along the weld bead direction.

If (Z>0), q(X, Y, Z) will be expressed as follow :
$$q_1(X,Y,Z) = \frac{6\sqrt{3}f_f Q}{a_1 bc\pi\sqrt{\pi}} e^{-3X^2/b^2} e^{-3Y^2/c^2} e^{-3Z^2/a_1^2} \tag{1}$$

If (Z≤0), q(X, Y, Z) will be expressed as follow :
$$q_2(X,Y,Z) = \frac{6\sqrt{3}f_r Q}{a_2 bc\pi\sqrt{\pi}} e^{-3X^2/b^2} e^{-3Y^2/c^2} e^{-3Z^2/a_2^2} \tag{2}$$

Where,

f_f, f_r: factors affecting the amount of heat produced by the area defined by (Z>0) and area defined by (Z≤0). The sum of f_f and f_r must be equal to (2).

a_1, a_2, b, c: Parameters used to define the heat source volume (v).

Q: heat transferred to the weld pool.

Based on the obtained temperature field (T(x,y,z,t)), the mechanical model in Figure 4, is used to evaluate thermal strain $\varepsilon_{ij}(x,y,z,t)$ and consequently, the stress field evolution $\sigma_{ij}(x,y,z,t)$. Parameters describing mechanical behaviour depend on the temperature, as can be shown in Table 1.
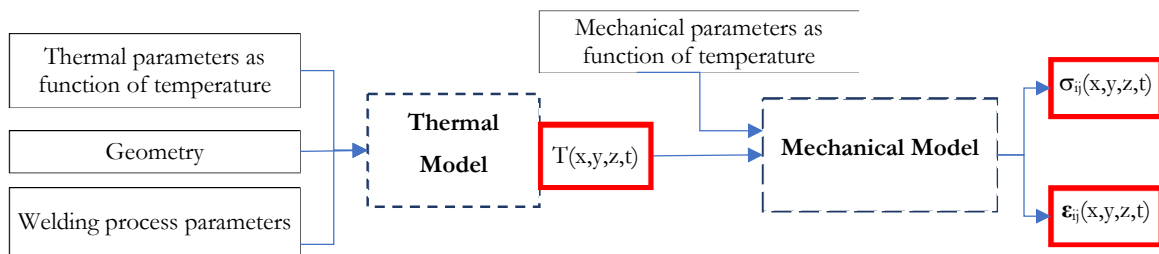

Figure 4. Structure of the thermomechanical model

Table 1. Mechanical and thermal parameters as a function of temperature

Temperature (°C)	24	200	600	800	1200	1480
Conductivity (W/m°C)	51	48	37	26	28	50
Convection factor (W/m²°C)	9,5	16,3	54,8	90,8	208,1	340,8
Young's modulus (GPa)	205	195	88	75	60	17
Yield strength (MPa)	364	280	55	40	7	0,01
Coefficient of expansion (10⁻⁶/°C)	12,18	12,66	14,41	12,61	13,37	13,37

2.1 Results of the Thermomechanical Model

The thermomechanical problem is solved using an APDL (Ansys Parametric Design Language) programs, which allows to create the ellipsoidal volume of the heat source and produce the heat density using the Gaussian distribution.

This volume move along the weld bead using the speed already specified. The program is responsible for the execution of the thermal then mechanical solver at each time step. The results show that the temperatures at the interface between the two welded parts exceed the melting temperature of steel (1500 °C),as in Figure 5. This validates the welding parameters and ensure a continuous bond at the entire contact surface. The lowest temperature at the interface is 1761°C, and the highest is 1979 °C.
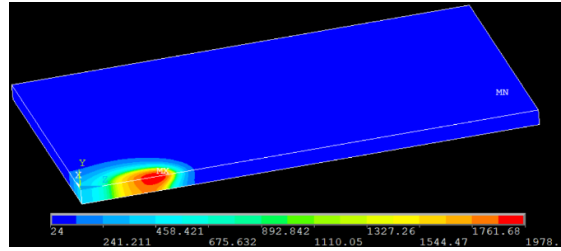

Figure 5. Temperature field produced by welding

The stress field obtained after the cooling of the welded plates is defined as the residual stress field, and it is denoted by $\sigma^r_{ij}(x,y,z)$. The analysis of the obtained results shows that the residual stress state can be considered a plan stress state with two predominant components along the x and z axes. This can be explained by the geometry of the plate and the welding line. Thus, the analysis of this field can be summarised by analysing the two components, (σ^r_{xx}) called the transverse residual stress and (σ^r_{zz}) called longitudinal residual stress. The components (σ^r_{zz}) have the highest value of 296 MPa as in Figure 6(a). However, the (σ^r_{xx}) component reaches a maximum value of 217 MPa, Figure 6(b).
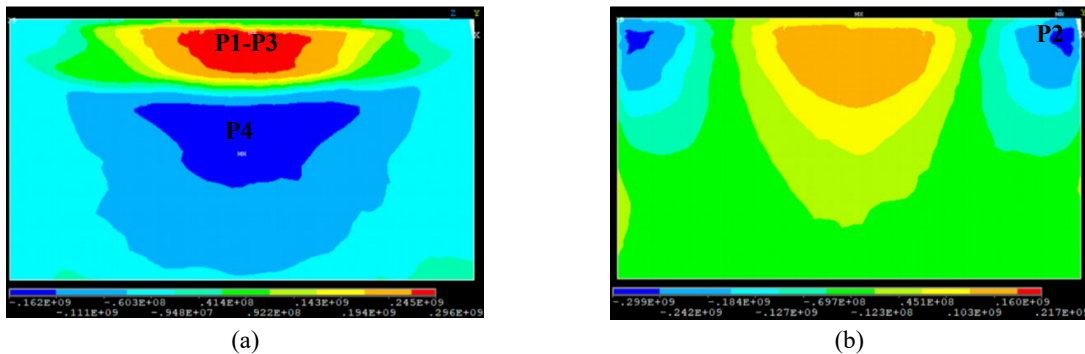

(a)   (b)

Figure 6. (a) Longitudinal residual stress (σ^r_{zz}) and (b) transverse residual stress (σ^r_{xx})

To analyse the relaxation process, we identify the most loaded areas by residual stresses (Table 2), which help us to identify the level of stress needed to initiate relaxation. Noting that the areas where the residual stresses (σ^r_{xx}) and (σ^r_{zz}) are maximum, as identified by the points (P1) and (P3), these points are located in very close zones and can be considered at the same zone.

Table 2. Location of the points presenting the maximum and minimum stresses in both x and z directions

	σ^r_{xx}(MPa)	σ^r_{yy}(MPa)	σ^r_{zz}(MPa)	τ^r_{xy}(MPa)	τ^r_{yz}(MPa)	τ^r_{xz}(MPa)	Point position		
							x (mm)	y (mm)	z (mm)
P1	217,3	17,9	276,9	-2,0	-2,0	-0,5	0	-1,7	73
P2	-299,2	-20,2	-12,8	2,8	1,4	0,6	0	-1,7	8
P3	167,3	1,3	295,6	2,37	-0,42	-0,3	6	0	72,7
P4	19,5	-3,0	-162,0	-0,2	0,4	12,6	50	-5	80

3.0 MODELLING OF THE RELAXATION PROCESS

3.1 *Multiaxial Hardening Models*

Residual stress relaxation can be achieved after plastic strain, which depends on the behaviour of the material [18]. The elastic domain in the stress space is not stable in the case of strain-hardening materials, and it depends on the loading history. Under repeated loads, the resolution of the stress and strain field requires the identification of the elastic domain during each load cycle. The evolution of this domain affect the plastic deformations and the residual stress relaxation. The evolution laws of the elastic domain and the constitutive law in the plastic regime were derived from the plasticity theory, mainly based on the theory of (J2) using the equivalent stress of Von Mises to formulate the flow rule and the load function. Several models can be used to evaluate strain hardening and the location of the elastic domain in the stress space. The two main idealised models used to describe the hardening process are the isotopic and kinematic models [19]-

[22]. Based on the previous models, authors combine linearly and non-linearly isotropic and kinematic hardening to increase the accuracy of the results [23]-[25].

To define load function (F) which gives the elastic domain position in the stress space, we use a tensor (α_{ij}) to describe kinematic hardening. A scalar (K) is used to describe isotopic hardening. Under these two hardening processes, the load function (F) can be expressed as follows:

$$F = \sqrt{\frac{3}{2}(s-\alpha):(s-\alpha)} - K \tag{3}$$

where, K is scalar describing isotropic hardening, s is stress deviator tensor, and α is back stress tensor.

Isotropic hardening

Isotropic hardening describe the extension of the elastic domain in the stress space [26] using a scalar (K) which can be expressed in terms of the accumulation of the plastic strain (p).

$$\dot{p} = \sqrt{\frac{2}{3}\dot{\varepsilon}^p : \dot{\varepsilon}^p} \tag{4}$$

The Voce model [27] is used to define the relation between (K) and (p):

$$K = \sigma_0 + R_0 p + R_\infty \left[1 - \exp(-bp)\right] \tag{5}$$

where, σ_0 is the initial yield strength and R_0, R_∞, b are material parameters.

Kinematic hardening

Describing the elastic domain by just using kinematic hardening is not realistic under cyclic load due to the variation of the applied load (tension and compression) [28]. In addition to the expansion, the elastic domain can be displaced in the stress space under plastic strain. To describe the new position of the elastic domain, a second-order tensor (α) is used. This tensor describes the new position of the hydrostatic axis in the stress space after plastic strain. A linear model [29] can relate the evolution of (α) to the evolution of the plastic strain tensor.

$$d\alpha_{ij} = C.d\varepsilon_{ij}^p \tag{6}$$

where C is scalar factor related to the material. A nonlinear model proposed by Armstrong and Frederick [28] allows for taking into account the saturation of the hardening tensor, α_{ij}.

$$d\alpha_{ij} = \frac{2}{3}Cd\varepsilon_{ij}^p - \gamma\alpha_{ij}d\hat{\varepsilon}^p \tag{7}$$

where, $\hat{\varepsilon}^p$ is the equivalent plastic strain, and γ, C are parameters related to the material

$$\hat{\varepsilon}^p = \sqrt{\frac{2}{3}\left(\varepsilon^P : \varepsilon^P\right)} \tag{8}$$

Chaboche [30] proposes a new model using a superposition of the previous expression, this allows to describe the hardening process over a large domain of plastic strain.

$$\alpha_{ij} = \sum_{k=1}^{M}\left(\alpha_{ij}\right)_k \tag{9}$$

Each tensor (α_{ij})k respects the differential equation below:

$$d\left(\alpha_{ij}\right)_k = \frac{2}{3}C_k d\varepsilon_{ij}^p - \gamma_k\left(\alpha_{ij}\right)_k d\hat{\varepsilon}^p \tag{10}$$

Subsequently, Chaboche and Voce models were adopted for the description of kinematic and isotropic hardening. Experimental results [31] obtained by mechanical tests on S355 steel are listed in Table 3. The hardening parameters in the table were considered insensitive to the temperature during the relaxation modelling.

Table 3. Material parameters

Parameters of elastic behaviour	Young's modulus (E)	185000MPa
	Poisson ratio (ν)	0.3
Isotropic hardening parameters (Voce model)	σ_0	386 MPa
	R_0	0 MPa
	R_∞	20.8 MPa
	B	3.2
Kinematic hardening parameters (Chaboche model) (k=3)	C_1	5327MPa
	γ_1	75
	C_2	1725 MPa
	γ_2	16
	C_3	1120 MPa
	γ_3	10

3.2 Approach Used to Model the Residual Stress Relaxation

To model stress relaxation, a new numerical model was built to follow the evolution of the internal stresses during and at the end of the application of an external cyclic load. Thus, the first step consists in extracting the stress state resulting from the thermomechanical model obtained at the end of cooling in a file that defines the stress tensor at each node (Figure 7). Subsequently, an APDL subroutine using the INISTAT function was used to define at each node of the new model, an initial stress state. The mesh was built keeping the same node positions used in the thermomechanical model.
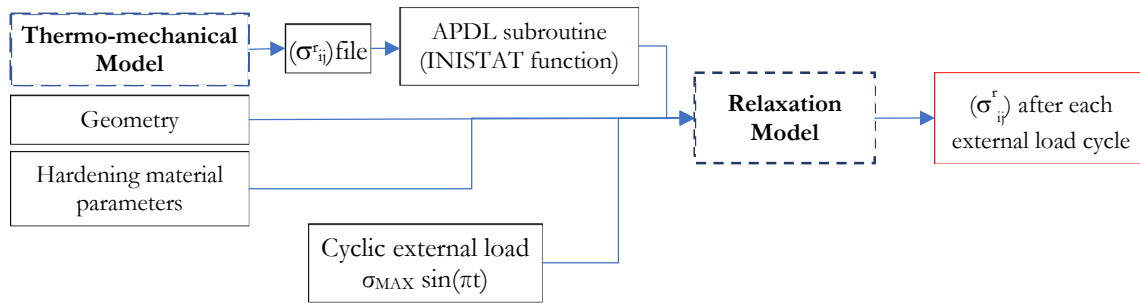
Figure 7. Structure of the relaxation model

In this part, we initially evaluate the impact of the cyclic external load applied on surface A2 (Figure 8), and thereafter, the effect of the cyclic load applied on A1 to deduce the required load level needed to initiate the relaxation process, the areas affected by relaxation and the relaxation rate. Each external load will be sinusoidal pressure normally applied on one surface:

$$\sigma_T(t) = \sigma_{TMAX}\sin(\pi t) \quad - \quad \text{Transverse load pressure applied on A1} \tag{11}$$

$$\sigma_L(t) = \sigma_{LMAX}\sin(\pi t) \quad - \quad \text{Longitudinal load pressure applied on A2} \tag{12}$$
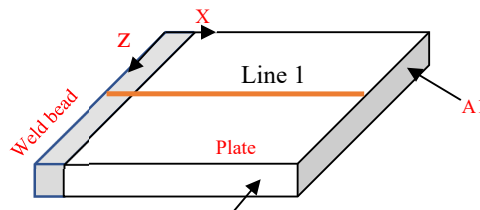
Figure 8. Surfaces subjected to external loads

Using these results, it is possible to decide in a design project whether to take into consideration the relaxation effect or not. If the load required to initiate the relaxation is high and approaches the yield strength of the material, we can judge that the state of the residual stresses remains stable and can be regarded as an average constant loading. Otherwise, the designer will have to break down the fatigue life of the structure into two phases. The first phase is where the relaxation of the residual stresses takes place, and the second phase is after the relaxation. In fracture mechanics, these results decide whether the residual stresses remain stable at the crack tips where the stress level exceeds the elastic limit. Thus, the first

objective of this part is to analyse the external load (σ_0) required to initiate the relaxation process. The second objective is to analyse the evolution of the residual stresses after the applications of various levels of external load which exceed the stress limit (σ_0) required to initiate the relaxation.

3.3   Relaxation under Longitudinal Load (Normal to A2)

During this part, we impose an external longitudinal load $\sigma_L(t)$ on the surface (A2) as follows:

$$\sigma_L(t)= 300 \sin(\pi t) \text{ (MPa)} \tag{13}$$

To investigate the mechanisms of the relaxation process and the influence of the plastic strain, we evaluate the stress tensor at the point (K) defined by its location (X_K=6mm, Y_K=0mm, Z_K=73mm), which is subjected to the maximum value of the residual stress (σ^r_{zz}). $\sigma_{ij}(K,t)$ is the stress tensor obtained on point (K) at time (t). When no external load is applied (t=0), the stress tensor is expressed as below:

$$\sigma(K,0) = \begin{pmatrix} 167 & 2.4 & -0.3 \\ 2.4 & 1.3 & -0.4 \\ -0.3 & -0.4 & 295.6 \end{pmatrix} MPa \tag{14}$$

The initial residual stress state can be assimilated as a plane stress state, and the principal stress axis is (X) and (Z). At the beginning of the load application (t<0.2s) (Figure 9), $\sigma_{xx}(K,t)$ remains stable during the elastic state with a value of 167 MPa, and the stress $\sigma_{zz}(K,t)$ calculated by the FE solver approach the stress calculated by the addition of the initial residual stress (σ^r_{zz}) and the external load (σ_L) with a relative difference of 2%. Using Von Mises criterion, $\sigma_{zz}(K,t)$ must exceed a value of 441.5MPa in order to introduce plastic strain. Using numerical results, the beginning of the relaxation process appears when $\sigma_{zz}(K,t)$ exceeds 423 MPa. In Figure 9, we plot $\sigma_{zz}(K,t)$ stress and the external load $\sigma_L(t)$. We also plot $\Delta\sigma(t)=\sigma_{zz}(K,t)-\sigma_L(t)$, the evolution of this difference reveals the beginning of the relaxation.
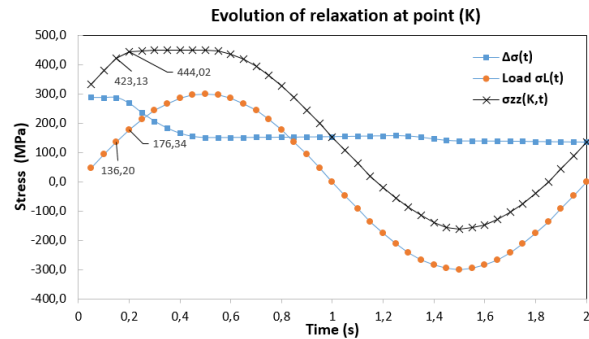

Figure 9. External load and stress at point (K)

Figure 10 shows the areas affected by the plastic strain at two moments (0,2s and 1.5s). The zone affected by the plastic strain during the tensile cycle at (0.2s) is located in the area where the initial residual stress (σ^r_{zz}) is at the maximum value. During the compression cycle at (1.5 s), we observe the formation of the plastic strain at the location where the initial residual stress (σ^r_{zz}) is at a compression state.
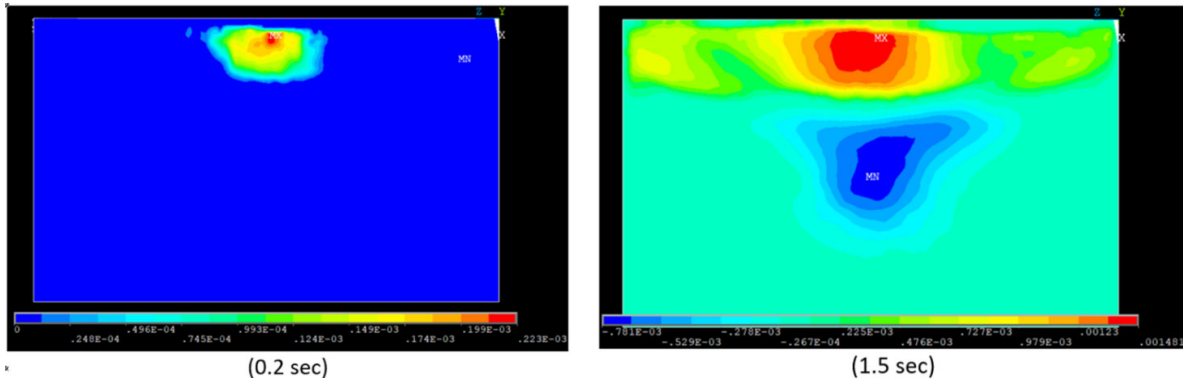

Figure 10. Evolution of the plastic strain (εpzz) at different times of the load cycle

At the beginning of load application, the difference ($\Delta\sigma$) is stable as long as the behaviour of the material remains elastic. Where (t=0.2s), the relaxation process is activated, which can be confirmed by a decrease of ($\Delta\sigma$) due to the plastic strain. After the external load has reached its maximum value, ($\Delta\sigma$) is stabilised again. Through the compression phase,

($\sigma_L(t)<0$), ($\Delta\sigma$) preserve a stable value until t=1.35s where the relaxation process is activated again under compression which produces plastic strain in zone 2 (Figure 11).
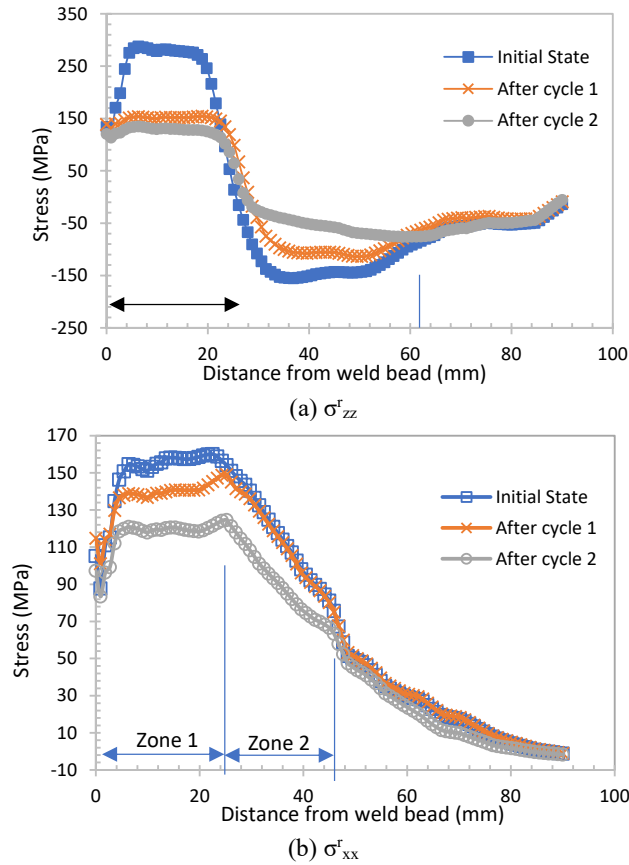

(a) σ^r_{zz}

(b) σ^r_{xx}

Figure 11. Residual stress on line 1 after longitudinal load cycles

To analyse the evolution of the relaxation process, we plot σ^r_{zz} and σ^r_{xx} observed on line 1 after the tensile and compression cycle (Figure 11). After the first tensile cycle, the maximum value of the (σ^r_{zz}) stress observed on line 1 dropped from 296MPa to 150 MPa. After a second compression load, the residual stress is subjected to a further drop but with low value. These results confirm that the relaxation is a damped process, and the residual stress will remain stable after a few numbers of load cycles. It is imperative to highlight that the application of high intensity of the external load in the longitudinal orientation allows the reduction of the intensity of the residual stresses, which are the results of an important plastic strain that can be a source of the damage initiation near the welding defects [32].

We can see in Figure 10 and Figure 11 that the area affected by an important amount of plastic strain is the area subjected to an important rate of relaxation. The observation of the evolution of the residual stress (σ^r_{xx}) shows a localised relaxation in the vicinity of the weld bead. The maximum value of residual stress (σ^r_{xx}) on line 1 drops from 160 MPa to 149 MPa after the first tensile cycle. We obtained a similar stress drop to 121 MPa after the second compression cycle. It can be seen that the relaxation process is different between zones 1 and 2. Zone 1 is affected by a relaxation process during tensile and compression load cycles. However, Zone 2 is affected by relaxation during compression only. Thus, under longitudinal load, the effect of the compression cycle on (σ^r_{xx}) stress remains greater than the effect of the tensile cycle.

3.4   Relaxation under Transverse Load (Normal to A1)

Unlike longitudinal load, the relaxation process under a transverse load (along the x-axis) takes place in the middle of the plate, further from the weld bead. The initiation of relaxation takes place as soon as the external load reaches a value of 171.8 MPa. Figure 12 shows that the initiation of the plastic strain is located at the area which presents a high compressive state of (σ^r_{zz}) at point (P4). At this location, the difference between the stress tensor components (σ_{xx}) and (σ_{zz}) is high, which amplifies the (J2) invariant under tensile transverse load. Figure 12 shows the evolution of (σ^r_{zz}) and (σ^r_{xx}) on line 1 after each cycle of the transverse load.
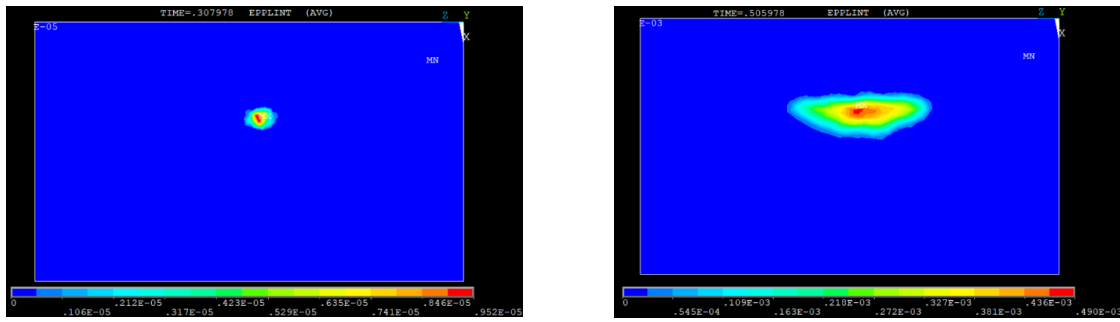
$$\sigma_T(t)= 300 \sin(\pi t) \text{ (MPa)} \tag{15}$$

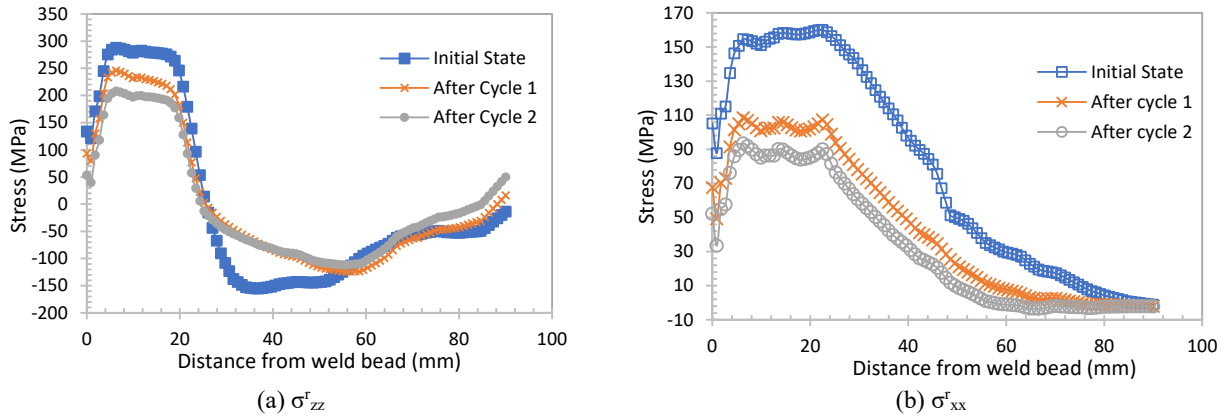Figure 12. Plasticity initiation zone under transverse load

(a) σ^r_{zz}

(b) σ^r_{xx}

Figure 13. Residual stress on line 1 after transverse load cycles

Under transverse load, the relaxation of σ^r_{zz} is less important than that obtained under longitudinal load. The maximum value of this stress on line 1 drops to 207 MPa after the second cycle instead of 150 MPa obtained under longitudinal load. However, the drop of σ^r_{xx} is more important in this load case; the maximum value of this stress falls towards 93.4 MPa after the two cycles, while this stress has reached a value of 120 MPa under a longitudinal load.

The comparison of the obtained results for the two load cases shows that the most influenced residual stress is oriented along the direction of the external applied load. Figure 14 shows the evolution of each residual stress (σ^r_{zz} and σ^r_{xx}) as well as its drop after each loading mode under a stress amplitude of 300 MPa. The drop is calculated as the difference between the initial and final state.

(a) σ^r_{zz}
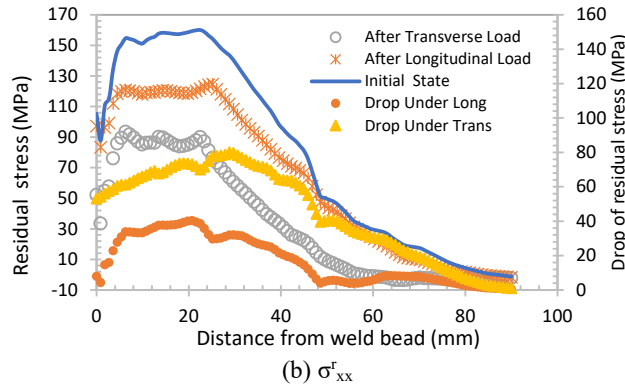
(b) σ^r_{xx}
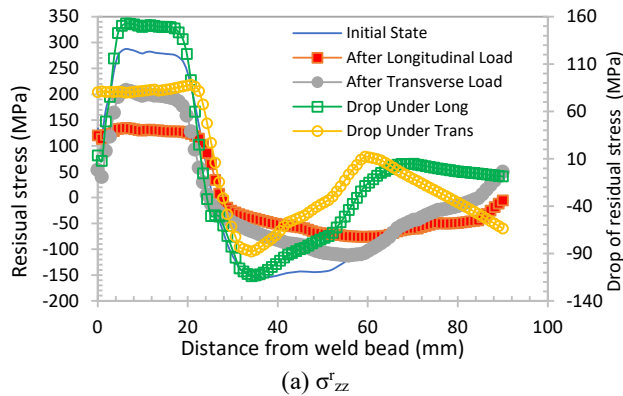
Figure 14. Effect of load orientation on the relaxation of the residual stresses

To analyse the relation between relaxation rates and the applied load, we present in the following part the evolution of the relaxation rate (Rr) of each residual stress according to the applied load. The relaxation rate (Rr) of each residual stress (σ^r_{xx} or σ^r_{zz}) is calculated according to the following expression:

$$Rr_{xx} = \frac{\sigma^{r0}_{xx} - \sigma^{rN}_{xx}}{\sigma^{r0}_{xx}} \quad Rr_{zz} = \frac{\sigma^{r0}_{zz} - \sigma^{rN}_{zz}}{\sigma^{r0}_{zz}} \tag{16}$$

where, Rr_{xx} is relaxation rate of σ^r_{xx}, Rr_{zz} is relaxation rate of σ^r_{zz}, σ^{r0}_{xx}, σ^{r0}_{zz} is the maximum value of residual stresses (σ^r_{xx}, σ^r_{zz}) on the plates at initial state (before relaxation), σ^{rN}_{xx}, σ^{rN}_{zz} is the maximum value of residual stresses (σ^r_{xx}, σ^r_{zz}) on the plates after several load cycles (after relaxation). The evolution of the relaxation rate (Rr) was analysed according to the applied load rate (Lr), which is calculated by the following expression.

$$Lr = \frac{\sigma_A}{Re} \tag{17}$$

where σ_A is amplitude of external load applied, and Re is yield strength.
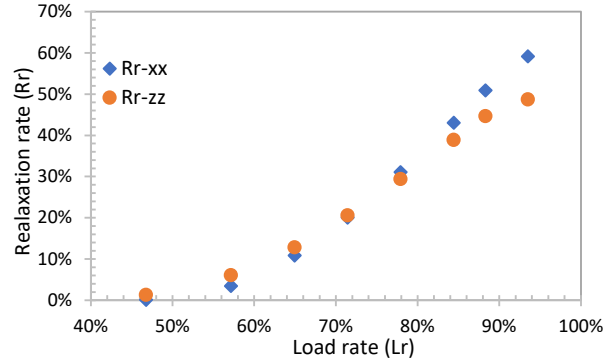
In this part, the relaxation rate is analysed when the applied load amplitude varies between 47% and 94% of the yield stress, as shown in Figure 15. These values are the typical load level considered to design a steel structure subjected to static or cyclic loads. Under longitudinal load, the relaxation rate of (σ^r_{zz}) is approaching 80 % if the applied load approaches the yield limit. The residual stresses (σ^r_{xx}) have a relaxation rate that does not exceed 40%. Under transverse load, it can be seen that the evolution of the relaxation rate of the two residual stresses does not show much difference. Residual stress (σ^r_{zz}) can reach a relaxation rate of 50%, and σ^r_{xx} can reach 60% when the applied load is in the vicinity of the yield limit. Also, note that the relaxation process is initiated when the applied load reaches a value between 45% and 47% of the yield strength, depending on the orientation of the applied load.

Thus, the orientation of the external load has a considerable influence on the relaxation process. However, this influence depends on the intensity of the applied load. At low loading levels of less than 55 % of the yield limit, the effect of direction is negligible and similar behaviour is observed for the longitudinal and transverse load. As the load values exceed 55% of the yield limit, the orientation of the load has a considerable influence on the relaxation progress. The application of longitudinal load quickly eliminates a high amount of residual stress (σ^r_{zz}). However, transverse load retains considerable values of residual stresses even if the applied load reaches the yield limit.

Thus, under a low level of external load, it is possible to consider that residual stresses are in a stable state. Thus, the local stress state will be the superposition of the stress state produced by the external load and the state of residual stresses. Noting that the endurance limits of welded joints given by the IIW or by the Eurocode 3 generally vary between 80 and 160 MPa [33]. This confirms that the relaxation process may not be observed under uniaxial load applied on steel structures designed using the previous design standards to ensure fatigue strength.
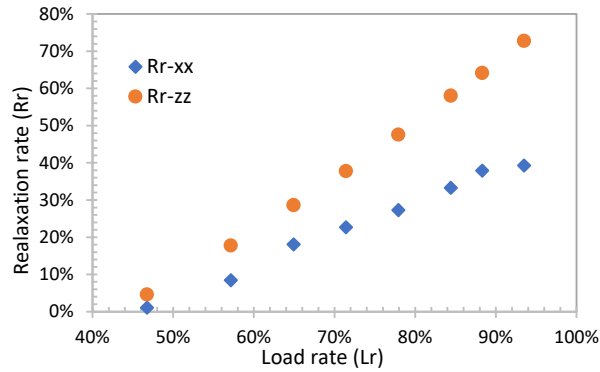
(a) relaxation rate under longitudinal load

(b) relaxation rate under transverse load

Figure 15. Evolution of the relaxation rate as a function of the applied load rate
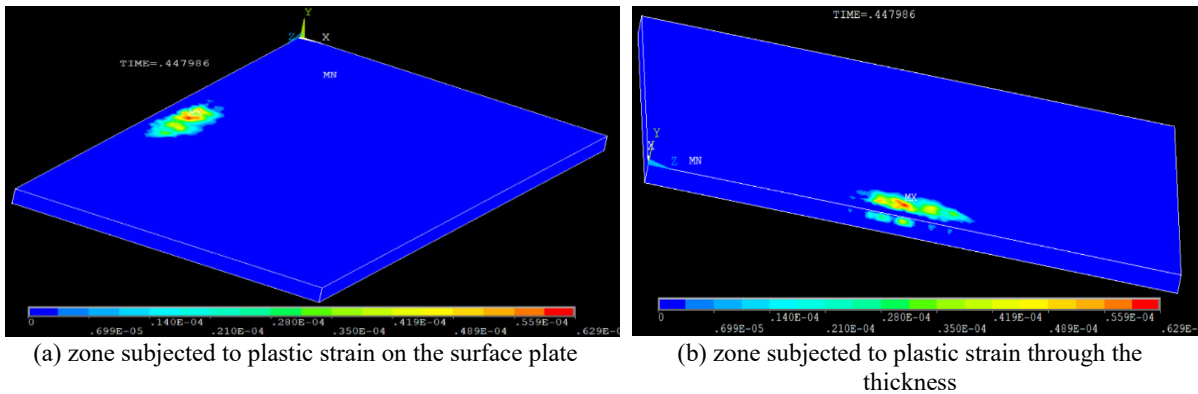
3.5   Relaxation under Bi-Axial Load

In this part, we will analyse the initiation and evolution of the relaxation process when a biaxial external load is applied. External load (σ_T) is applied normally to (A1); simultaneously, a second load (σ_L) is applied to (A2). The φ parameter is the phase between $\sigma_L(t)$ and $\sigma_T(t)$. The two loads will have the same amplitude (σ_a).

$$\sigma_L(t) = \sigma_a \sin(\pi t) - \text{ Longitudinal load applied on A2} \qquad (18)$$

$$\sigma_T(t) = \sigma_a \sin(\pi t + \varphi) - \text{ Transverse load applied on A1} \qquad (19)$$

Initiation of the relaxation process

The first results were obtained when the two applied loads are in phase ($\varphi=0°$) ($\sigma_L(t)=\sigma_T(t)$). The results show that the relaxation process is initiated when the external load reaches a value of 132 MPa, and the relaxation initiation zone is located at points (P1) and (P3) where the initial residual stresses (σ^r_{xx} and σ^r_{zz}) are the greatest (Figure 16).

(a) zone subjected to plastic strain on the surface plate

(b) zone subjected to plastic strain through the thickness

Figure 16. Zone subjected to plastic strain producing relaxation process under in-phase bi-axial load

The load intensity required for relaxation (132 MPa) is significantly lower than the levels observed for a uniaxial load state. Thus, even for some welded structures respecting the design standard and providing fatigue strength, it is possible to initiate the relaxation process under this load configuration.

The second results are obtained by applying (σ_T) on (A1) and (σ_L) on (A2). The phase between the two loads is ($\varphi=180°$) ($\sigma_L(t) = -\sigma_T(t)$). In this case, the plastic strain is initiated on the edge of the plates in the vicinity of the point (P2) (Figure 17). The analysis of the results shows that the relaxation is initiated at a low level of the external load, which is 68.9 MPa. Therefore, the effect of phase shifts between the loads is essential. Noting that the amount of relaxation, if the external load reaches the limit value of 80 MPa, it is not very significant.
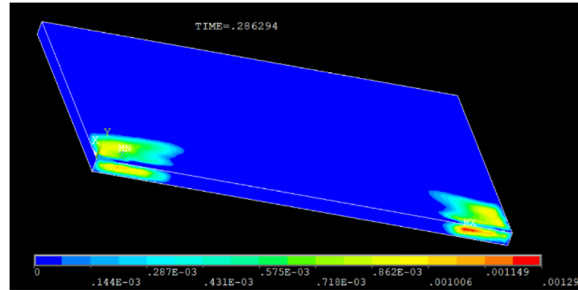

Figure 17. Zones subjected to plastic strain under out-of-phase bi-axial load

Evolution of stress relaxation

To estimate the evolution of the relaxation process, we initially analyse the effect of different modes of biaxial load on residual stresses in order to identify the critical loading mode which has the highest impact on the residual stress state. Each mode is identified by the angle phase (φ). Longitudinal and transverse loads have the same amplitude:

$$\sigma_L(t) = \sigma_a \sin(\omega t) \text{ and } \sigma_T(t) = \sigma_a \sin(\omega t + \varphi) \tag{20}$$

The observation of the previous results under uniaxial load confirms that the relaxation requires initiation of plastic strain. Thus, to identify the bi-axial configuration having a maximum impact on the residual stress state, we proceed with a local analysis of the effect of the stress tensor $\sigma_{ij}(K,t)$ at a point (K) on the plastic strain. Thus, we analyse a biaxial plane stress state presenting two principal axes (x) and (z), where the two components ($\sigma_{xx}(t)$, $\sigma_{zz}(t)$) present a sinusoidal evolution with a phase shift (φ), the two components are considered to have the same amplitude.

$$\sigma_{xx}(t) = \sigma_A \sin(\omega t) \quad \text{and} \quad \sigma_{zz}(t,\varphi) = \sigma_A \sin(\omega t + \varphi) \quad \text{and} \quad \sigma_{yy}(t) = 0 \tag{21}$$

We initially proceed to analyse, locally, the phase shift (φ) between the two components ($\sigma_{xx}(t)$, $\sigma_{zz}(t)$), which maximises the equivalent stress (Von Mises stress) considering that the residual stresses are zero. The Von Mises equivalent stress is denoted $\sigma_{VM}(t,\varphi)$ and is a function of time (t) and phase shift (φ). Along each period cycle, the Von Mises equivalent stress $\sigma_{VM}(t,\varphi)$ reaches a maximum value which is denoted "Max($\sigma_{VM}(\varphi)$)"; this value depends on phase shift (φ).

$$\sigma_{VM}(t,\varphi) = \frac{1}{\sqrt{2}} \sqrt{\left(\sigma_{xx}(t) - \sigma_{yy}(t)\right)^2 + \left(\sigma_{xx}(t) - \sigma_{zz}(t,\varphi)\right)^2 + \left(\sigma_{yy}(t) - \sigma_{zz}(t,\varphi)\right)^2} \tag{22}$$

In the case where the two stresses $\sigma_{xx}(t)$ and $\sigma_{zz}(t,\varphi)$ are in phase ($\varphi=0$), it is possible to calculate "Max($\sigma_{VM}(\varphi=0)$)", the maximum value of the equivalent Von Mises stress $\sigma_{VM}(t,0)$:

$$\sigma_{VM}(t,\varphi=0) = \frac{1}{\sqrt{2}} \sqrt{\left(\sigma_A(\sin \omega t)\right)^2 + \left(\sigma_A(\sin \omega t)\right)^2} = \left|\sigma_A \sin \omega t\right|$$
$$Max\left(\sigma_{VM}(\varphi=0)\right) = \sigma_A \tag{23}$$

Thus, the plasticity criterion ($\varphi=0$): $\sigma_A \geq Re$. In the case where $\varphi=180°$, the maximum value of the Von Mises stress Max($\sigma_{VM}(\varphi=180°)$) can be obtained by:

$$\sigma_{VM}(t,180°) = \frac{1}{\sqrt{2}} \sqrt{\left(\sigma_A(\sin \omega t)\right)^2 + 4\left(\sigma_A(\sin \omega t)\right)^2 + \left(\sigma_A(\sin \omega t)\right)^2} = \sqrt{3}\left|\sigma_A(\sin \omega t)\right|$$
$$Max\left(\sigma_{VM}(\varphi=180°)\right) = \sqrt{3}\sigma_A \tag{24}$$

Thus, plasticity was initiated when the amplitude (σ_A), exceeds ($Re/\sqrt{3}$). Figure 18 allows us to determine the maximum value of the Von Mises stress Max($\sigma_{VM}(\varphi)$) for each phase shift (φ).
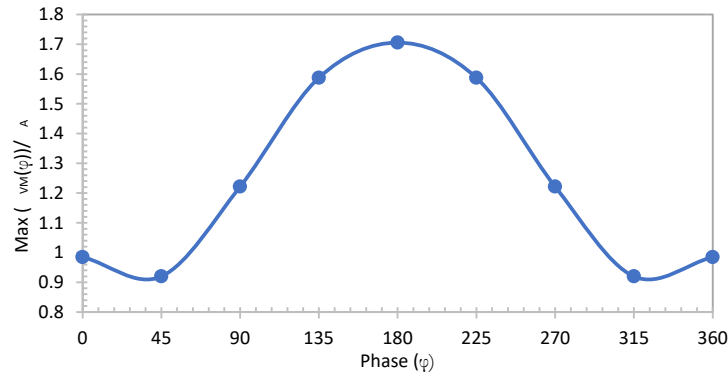
Figure 18. Extreme value of Von Mises stress as a function of φ

We can see that the maximum value of the Von Mises stress reaches its extreme value when the phase shift is 180°. Thus, this stress mode can be considered the most critical. In this case, it is sufficient that the stress amplitude reaches a value equal to ($Re/\sqrt{3}$ = 222 MPa) to initiate the relaxation process. Using the same methodology and by consideration the residual stresses, it is possible to predict the external load mode which has a considerable impact on the stability of the residual stresses. To conduct this analysis, a series of numerical models are used. In each model, the plates will be subjected to a biaxial external load ($\sigma_L(t)$ and $\sigma_T(t, \varphi)$) with a specific phase shift (φ). The load amplitude (σ_a) will be fixed at σ_a=230 MPa. For each phase shift value (φ), and after applying the bi-axial load, we identify through the obtained results, the maximum values of the residual stresses σ^r_{xx} and σ^r_{zz} remaining in the plates, and we calculate the relaxation rate of each residual stress.
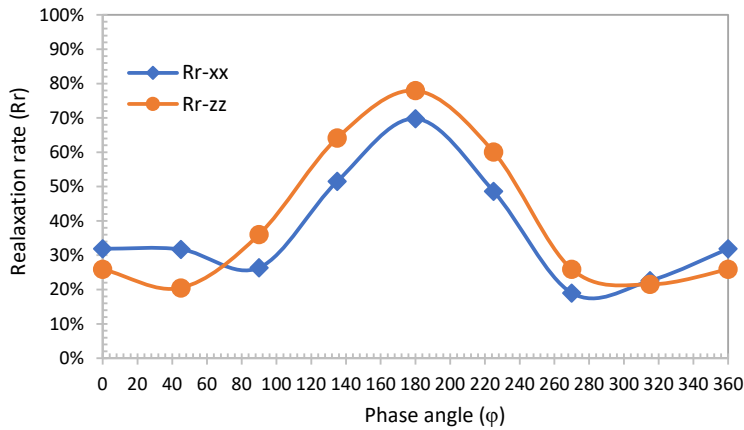

Figure 19. Evolution of the relaxation rate as a function of φ

The obtained results in Figure 19 confirm that the relaxation rate reaches its maximum value when the phase shift is 180°. Also, noting a slight difference between the relaxation rates of the two residual stresses (σ^r_{xx}, σ^r_{zz}). It is important to note that the effect of the phase shift on the relaxation rate presents a similar shape to the observed effect of the phase shift on the maximum value of the Von Mises stress Max($\sigma_{VM}(\varphi)$), this can lead to a proportional dependence between the maximum equivalent stress Max($\sigma_{VM}(\varphi)$) and the relaxation rate when the stress amplitude is around (σ_a=230 MPa). This observation is similar to that obtained under uniaxial load.

To verify the stability of the residual stresses, the critical biaxial loading mode (φ=180°) was considered. Several numerical analyses were carried out for different load amplitude (σ_a) to identify the evolution of the relaxation rate of each residual stress as a function of the load rate σ_a/Re. In the case of the most critical biaxial load, the initiation of relaxation takes place at low values of the load rate (16% of the yield stress Re). The relaxation process grows rapidly, and it can be seen that when the load rate reaches (65%) of the yield strength, 88% of the residual stresses are relaxed. The relaxation rate presents a saturation state, and it is limited to a value between 90% and 92% when the load rate reaches a value of 70 %. Even if the imposed load is important, the two residual stresses present permanent values of σ^r_{xx}=20 MPa and σ^r_{zz}=22 MPa.

Noting that the magnitude of the local stress required to initiate plasticity in this load case is 222 MPa, this value can be considered as the effective yield strength. In order to be able to compare these results with the results obtained under a uniaxial load, the effective load rate is calculated as the ratio between the amplitude σ_a and the effective yield strength σ_{ye}=222MPa, thus the value of the effective load rate (σ_a/σ_{ye}) is equal to (1) when the magnitude (σ_a) reached a value of

σ_{ye}=222MPa. This is the appropriate indicator of plastic strain initiation when no residual stresses take place. Figure 20 shows the evolution of the relaxation rate as a function of the effective load rate (ELr).
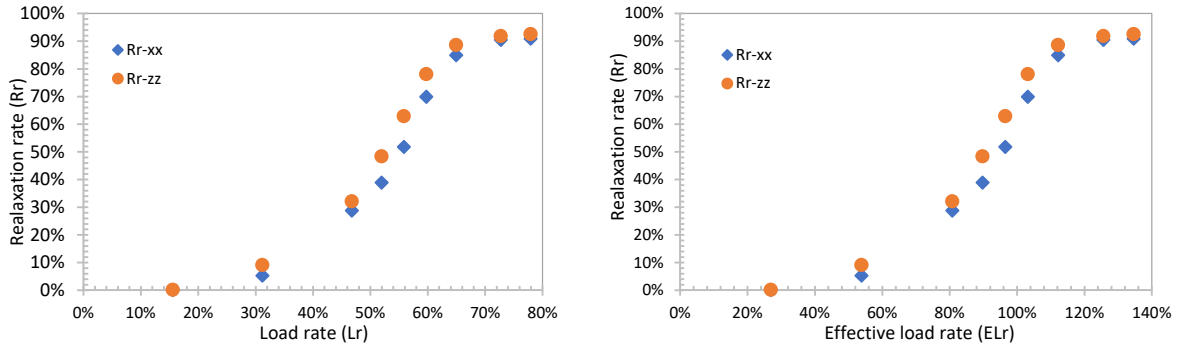

Figure 20. Evolution of the relaxation rate as a function of (a) load rate and (b) effective load rate

Observation of this curve shows a similar evolution to that obtained under uniaxial load. When the magnitude of the load approaches the effective elastic limit of 222MPa (ELr=1),\ the relaxation rate of σ^r_{zz} and σ^r_{xx} is respectively 63% and 52%. This allows us to generalise these results for uniaxial and biaxial load cases. Thus, in the case of a design project of steel structure, and after the evaluation of the external loads that the structure can support (based on yield criterion) by using a simple FE software without any consideration of residual stresses, we can estimate the maximum value of the relaxation rate in the but welded joints. The relaxation rate can reach a maximum value of 73% (relaxation rate of σ^r_{zz} under longitudinal external load). If the welded joint was subjected to yield stress, the minimum value of the relaxation rate that can be reached is 39% (relaxation rate of σ^r_{xx} under longitudinal load).

4.0   FATIGUE ANALYSIS OF WELDED JOINT

4.1   Analysis Procedure

The fatigue behaviour of the welded joint is described using (S-N) curves in a high cycle fatigue regime (HCF). The estimation of these curves was carried out by taking into consideration three main factors:

i.   The initial state of the residual stresses observed after welding;
ii.   The relaxation of the residual stresses generated after the hardening process;
iii.   The non-proportional stress state is produced by residual stress during load cycles.

Estimating the fatigue life of the welded joint subjected to cyclic load requires an analysis of the triaxial stress state. The (FE) resolution shows that the state of strain and stress is not cyclic during the first cycles of loading. Thus, it is mandatory to solve the state of stress and strains during several cycles of loading until the stress and strain tensors present a repeated cyclic state. To analyse the fatigue process, we consider a cyclic external load applied as considered before (a sinusoidal shape with a period of 2s). Further analysis (Figure 21) shows that the state of stress follows a cyclic regime after one or two cycles of application of the external load. Thus, it is possible to conduct a fatigue analysis on a stabilised cycle of stress and strain while neglecting the effect of the first cycles, where the state of stresses and strains is unstable due to the hardening process.
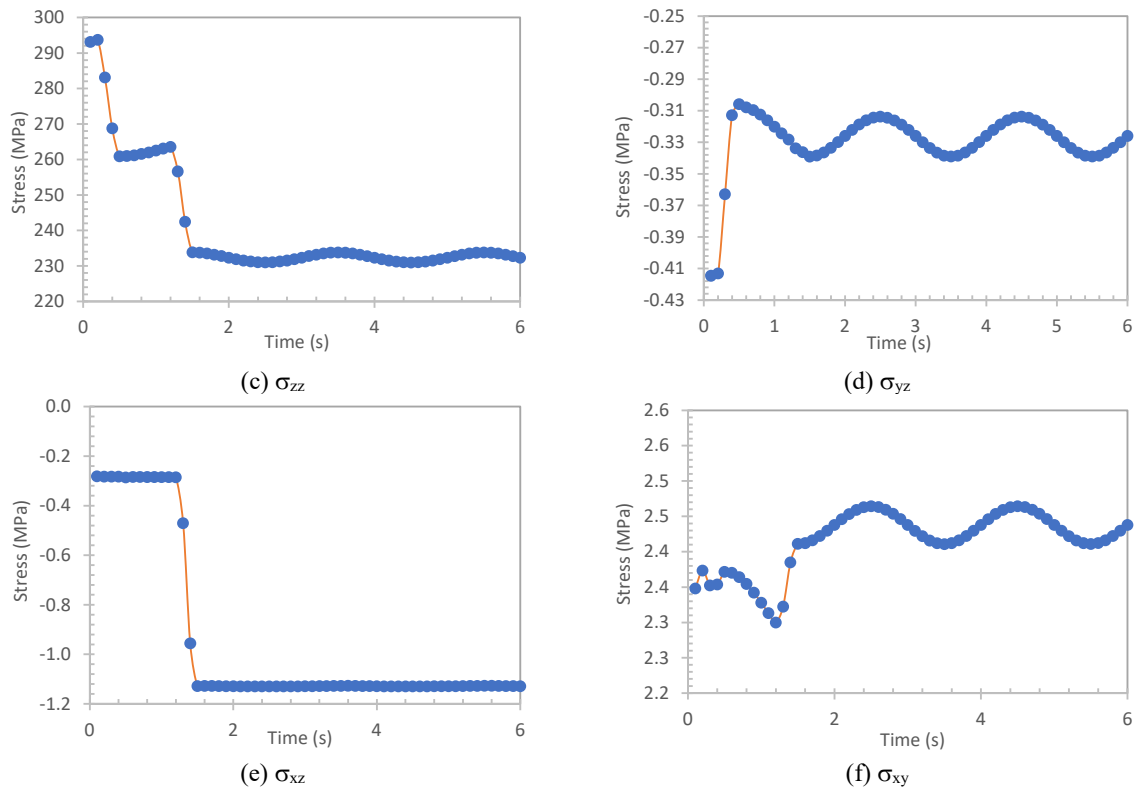

(a) σ_{xx} (b) σ_{yy}
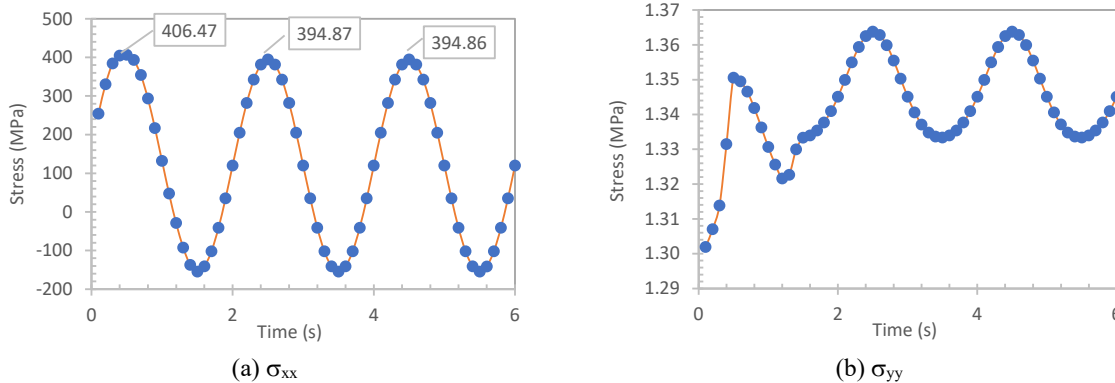
Figure 21. Evolution of the stress tensor components under transverse load (σ_a=275 MPa)

The fatigue analysis using a multiaxial model is necessary given the obtained state of the residual stresses. It is important to note that in the absence of external loads, residual stresses produce a plane stress state; this can be confirmed by observing Figure 21 where we can see the evolution of the six components of the stress tensor under a transverse load of 275 MPa at the point (P3) presenting the maximum value of residual stress (σ^r_{zz}).

The plot of σ_{zz} as a function of σ_{xx} between 4 and 6 seconds in Figure 22 shows that the stress state at the considered point is non-proportional. Under a transverse external load, the most significant stress (σ_{zz}) undergoes the greatest variation during the first loading cycles. It then stabilises around an average value of 232 MPa after the relaxation process. However, the component (σ_{xx}) undergoes a stabilised cyclic evolution after the first cycle.
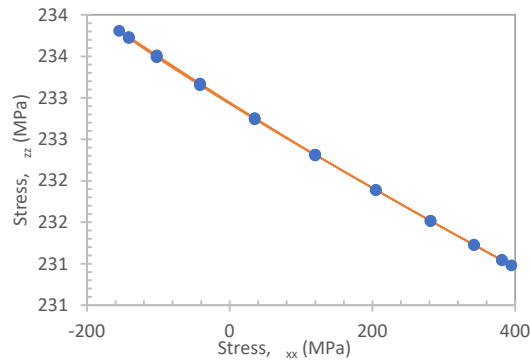

Figure 22. Evolution of σ_{zz} as a function of σ_{xx}

Noting that the two components (σ_{xx} and σ_{zz}) remain the most dominant during the majority of the loading cycles which shows that the principal stress axes present a stable state during the majority of the load cycle. After the end of the relaxation process, the elastic domain is extended and it becomes wider. Thus, the behaviour of the material becomes perfectly elastic, which shows that the fatigue analysis needs to be performed considering HCF regime.

4.2 Multiaxial Fatigue Analysis Approaches

Under a multiaxial stress state, several approaches can be applied to analyse the fatigue strength [34]-[36]. To choose which approach to use, several parameters need to be considered. The most fundamental parameters are the nature of the material, the damage mechanism, the proportionality of the stress state, and the fatigue regime (HCF,LCF). A review of

the research dealing with the fatigue of materials under a multiaxial stress state reveals several models that can be used to estimate fatigue life. The developed models aim to estimate only the number of cycles necessary for a microcrack initiation. The models proposed can be classified according to several approaches among which we can mention:

    i.   Approach based on equivalent stresses [37];
    ii.   Approach based on the triaxiality of the stress tensor [38],[39];
    iii.   Approach based on tensor invariants [40];
    iv.   Approach based on the theory of the critical plane [41]-[43].

Several experimental research [44],[45] show that models based on the critical plane approach come very close to experimental results. This justifies the significant development of new models [43],[46] using this approach. The accuracy of this approach finds its justification in the nature of the damage process of the crystalline materials [47]. This process takes place during gliding at grain crystals having one or more slip systems which are the most sensitive to the applied shear stress [48],[49]. In the case of polycrystalline materials, the grains on the free surface presenting a sensitive plane to the applied load will produce a slip defect that will propagate easily toward the free surfaces due to the lack of obstacles such as grain boundaries. The accumulation of these defects produces persistent slip bands (PSBs), which create promising sites for the initiation of microcracks [50]-[52]. Using an analogous analysis of this process, the approach of the critical plan tends to identify a critical plane submitted to maximum shear stress or strain or similar quantities.

Under the assumption that the stress tensor, which exhibits a maximum shear (stress or strain), is stable at a small volume (v) containing a sufficient number of grains, it is possible to admit that among the grains in the volume (v), one or more grains exhibit a promising orientation to the formation of slips defects, this defect will be able to propagate and to contribute to the formation of microcrack which produces a new two irregular surfaces in contact (Figure 23). The effect of the contact between the two surfaces produces friction which is responsible for slowing down the propagation thereafter. Under these conditions, the appearance of stresses or strain normal to the sliding planes reduce the effect of contact and further promotes the propagation process. This conclusion is validated by the experimental research work of Kaufman and Topper [53].
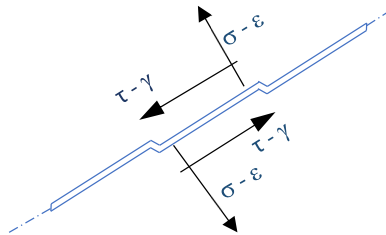

Figure 23. Initiation process of micro-crack under multiaxial stress

The results of Kaufman and Topper, show that when the plane of maximum shear is subjected to a normal compression stress, the variation of the normal stress does not affect the fatigue life. If the same plane is subjected to tensile stress, the evolution of this stress can considerably influence the fatigue life. In addition to these findings, the experimental results revealed that the average value of normal stress has an influence on fatigue life. These new results give experimental justification to the models already proposed in the 50s of the 20th century, such as the Findely model [54] [55] which defines the critical plane at a point as the plane maximising the linear combination between normal and shear stress.

$$\tau_{\theta A} + k\sigma_{\theta M} \tag{25}$$

where $\tau_{\theta A}$ is shear stress amplitude, $\sigma_{\theta M}$ is the maximum normal stress, k is the constant that depends on the material. For several cycles, N, Findely, proposes the following model. The expression gives the amplitude of the allowable shear stress, $\tau_{c\theta A}$, needed to initiate a microcrack after N cycles.

$$\tau_{c\theta A} = f - k\sigma_{\theta M} \tag{26}$$

This expression shows that the magnitude of the shear stress, $\tau_{c\theta A}$, required to achieve a fatigue life, N, depends on the maximum value of normal stress, $\sigma_{\theta M}$, applied to this plan. The increase of the normal stress considerably reduces the shear stress needed for the initiation of the microcrack, k is a factor that depends on the material and reflects its sensitivity to normal stress. Factor f can be seen as the shear stress needed to initiate a microcrack after N cycles when the normal stress is zero. It should be noted, however, that the application of the critical plane approach requires significant post-processing of a large mass of data obtained from finite element analysis. In addition to the identification of the stress and strain tensors at each node, it is necessary to add a series of additional analysis in each node in order to identify the most critical plane at the level of this node according to a predefined criterion. This analysis is carried out several times to follow the history of the evolution of the loads applied to this plan. In our calculation process, and at the level of each node, the angular position (α, β) of the normal vector ($\vec{n}$) to the analysed plane is used to identify each plane (Figure 24).
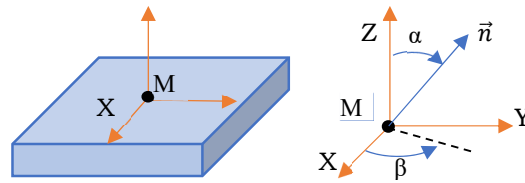
Figure 24. Angular parameters used to identify each plane

Evaluation of the damage on each critical plan is based on a function of the components of the stress or strain tensors or by using a variant of the strain energy [56]. It is important to note that each model based on the critical plane approach requires solving two main problems:

  i. Define a criterion for the identification of the critical plane;
  ii. Define a function allowing to evaluate the damage generated on the critical plane by the applied load.

This function relates the fatigue life (N) and the applied load on the critical plane through coefficients that depend on the material. These parameters can be identified through standard fatigue tests.

Fatemi – Socie Model

The Fatemi-Socie model (FS) is based on the critical plane approach [56] and provides satisfactory results [57]. It allows us to estimate the fatigue life by using a combination between the shear strain and normal stress. The critical plane in the case of the Fatemi-Socie model (FS) is subjected to maximum shear strain amplitude. The expression relating the applied load on the critical plane and the fatigue life is expressed as follows:

$$\frac{\Delta\gamma_{Max}}{2}\left(1+k\frac{\sigma_{n,Max}}{Re}\right)=\frac{\tau'_f}{G}\left(2N_f\right)^{b\gamma}+\gamma'_f\left(2N_f\right)^{c\gamma} \qquad (27)$$

where $\frac{\Delta\gamma_{Max}}{2}$ is the maximum amplitude of shear strain on the critical plane, k is sensitivity factor, $\sigma_{n,Max}$ is the maximum value of the normal stress acting on the critical plane, Re is yield strength of the material, τ'_f is shear fatigue strength coefficient, G is shear modulus, bγ is shear fatigue strength exponent, γ'_f is shear fatigue ductility coefficient, cγ is shear fatigue ductility exponent, 2Nf is number of reversals to failure.

According to the previous equation, the damage process requires the presence of a shear strain; thus, the presence of a pure hydrostatic load case cannot lead to any fatigue damage. In addition, if the shear strain is constant, the fatigue resistance is infinite which is in accordance with the insensitivity to the main shear stress. Identification of parameters $(\tau'_f, \gamma'_f, c\gamma, b\gamma)$ can be carried out by a torsion fatigue test where the stress normal to the critical plane is zero. The value of (k) can be obtained by adding a tensile fatigue test. If the fatigue parameters obtained by a tensile fatigue test are used, the previous expression can be expressed in the following form:

$$\frac{\Delta\gamma_{Max}}{2}\left(1+k\frac{\sigma_{n,Max}}{Re}\right)=(1+\upsilon_e)\frac{\sigma'_f}{E}(2N_f)^b+\frac{k}{2}(1+\upsilon_e)\frac{\left(\sigma'_f\right)^2}{E\,Re}(2N_f)^{2b}+(1+\upsilon_p)\varepsilon'_f(2N_f)^c+\frac{k}{2}(1+\upsilon_p)\frac{\varepsilon'_f\,\sigma'_f}{Re}(2N_f)^{b+c} \quad (28)$$

Where, ν_e is elastic Poisson's ratio, ν_p is plastic Poisson's ratio, σ'_f is fatigue strength coefficient, E is Young's modulus, ε'_f is fatigue ductility coefficient, b is fatigue strength exponent, c is fatigue ductility exponent. In order to estimate the fatigue strength, we use the fatigue properties of S355 steel obtained by Cruses et al. [58].

4.3   Numerical Analysis of the Fatigue Strength of Weld Joint

The main objective of the analysis is to build the (S-N) curve under a longitudinal and transverse loading mode. The obtained results allow us to evaluate the impact of the residual stresses on the fatigue behaviour and to check whether the load orientation has an effect on the fatigue curve or not. The amplitude of the imposed stress is lower than the yield stress because of the importance of the (HCF) regime for the design of steel structures. The external load will be considered sinusoidal with zero main value.

Estimation of k parameter

To assess the impact of residual stresses on fatigue strength according to the multiaxial fatigue criterion of Fatemi and Socie (FS), it will be necessary to identify the sensitivity parameter, *k*. According to the mechanical properties given in [58], it is possible to estimate the Wohler fatigue curve of the material (S355) according to the Smith, Watson and Topper Model (SWT). According to the same properties, it is possible to obtain the same curve by using the (FS) model, which requires the identification of the parameter (k). Figure 25 represents the (SN) curve obtained by the (FS) model for different values of *k* as well as the (S-N) curve obtained by the (SWT) model. The value of *k* is adopted that best approximates the (SN) curves of (SWT) and (FS) models.
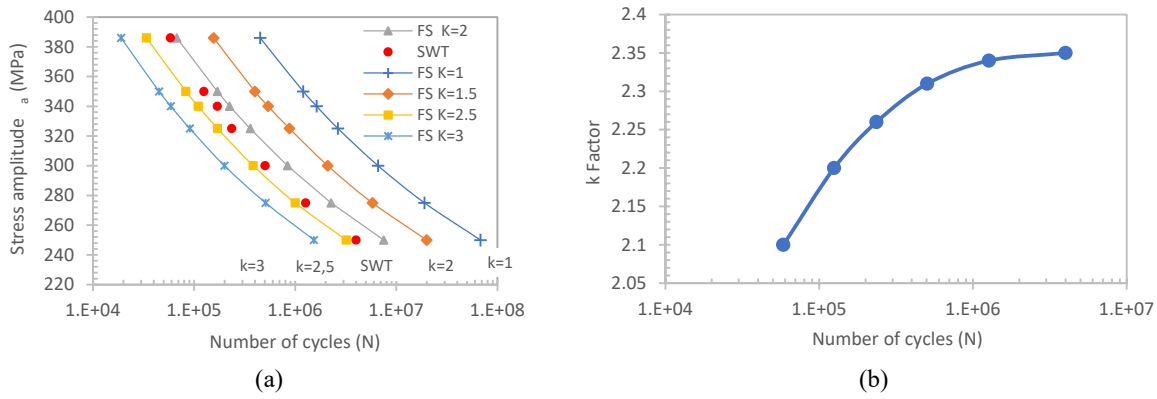
(a)   (b)

Figure 25. S-N curves obtained by the (a) FS and SWT models and evolution of the (b) sensitivity factor, *k*

The S-N curves obtained by the SWT model and the FS model show that the *k* factor ensuring reconciliation between the two models is between 2 and 2.5; shown in Figure 25. There is also a slight fluctuation in the value of the factor, *k*. Near the endurance limit, it is close to 2.5. However, it approaches 2 if the magnitude of the stress approaches the yield limit. Through the exact adjustment of the two models, SWT and FS, under uniaxial fatigue. It is possible to deduce the evolution of the factor, *k,* for each number of cycles, *N*. To construct the S-N curve, the load amplitude is taken at several values between 220 MPa to 360 MPa. The process of identifying each point on the S-N curve (shown in Figure 26) go through the following steps:

i. A constant amplitude load is applied for several cycles on the plate, presenting residual stress field.
ii. Using the finite element solver, the stress and strain field is calculated for the different nodes at different times after relaxation process.
iii. The algorithm for fatigue analysis evaluates the normal stress and shear strain applied to different planes during a load cycle.
iv. Through the previous results, we identify the critical plane subjected to a maximum shear strain amplitude as well as the maximum normal stress applied to this plane.
v. The factor, *k*, and the number of cycles, *N*, are estimated according to the Fatemi-Socie model.
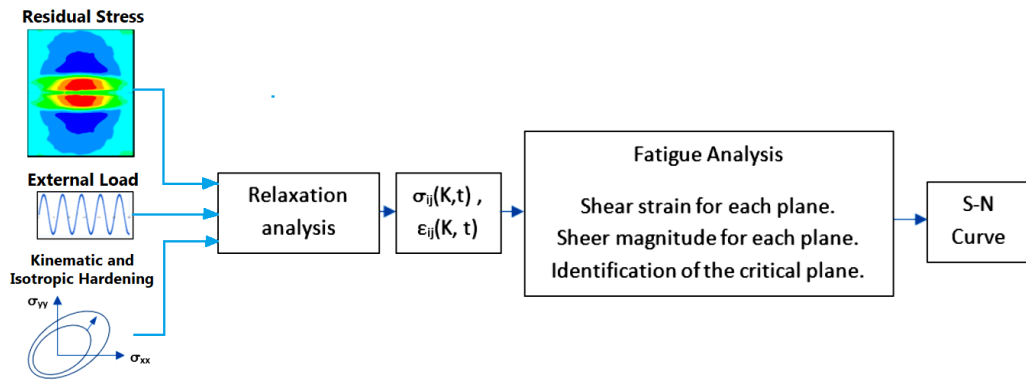

Figure 26. Approach for fatigue analysis

Effect of residual stresses under longitudinal and transverse load

Figure 27 shows the S-N curve of welded joint calculated by the FS model under longitudinal and transverse load and the (SN) curve of S355 previously obtained by SWT model. The S-N curve obtained under longitudinal load clearly shows the effect of residual stresses on the fatigue strength. It is important to note that the effect of these stresses changes according to the applied load. The effect of residual stresses on the fatigue strength is small when the amplitude of the longitudinal cyclic load approaches the yield strength; this can be justified by the results obtained previously, which show that the relaxation rate of the residual stresses (σ^r_{zz}) is significant when the applied load approaches the yield strength. The effect of residual stresses becomes clear for high fatigue life at a low load level. The endurance limit considered at 10^6 cycles shows a drop of 84 MPa. The maximum initial longitudinal residual stress (σ^r_{zz}) is 296 MPa. Thus, considering a superposition between the residual stress state and the stress field produced by the external load leads to a strong overestimation of the effect of the residual stresses on fatigue strength, this is due to the triaxial state of the residual stresses.
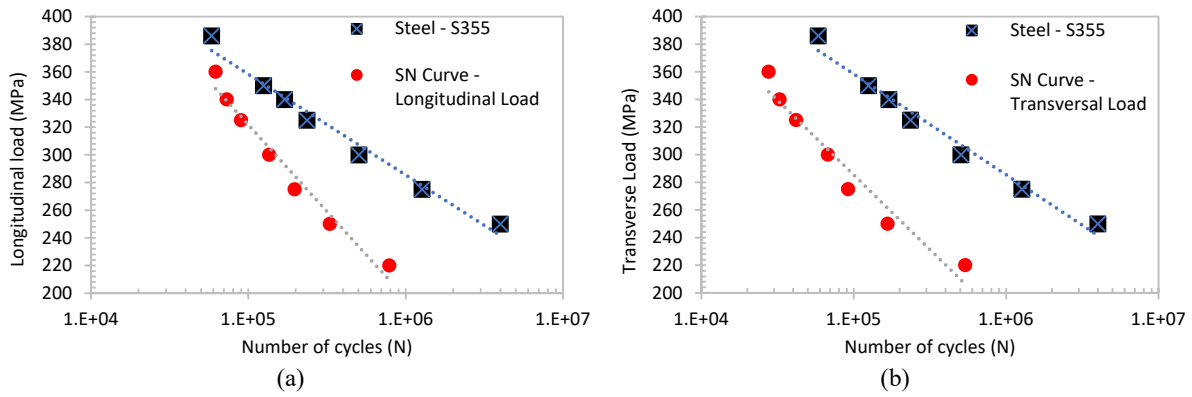
(a)   (b)

Figure 27. Effect of residual stress on S-N curve under (a) longitudinal and (b) transverse load

Under transverse load, the results show a more noticeable effect of residual stresses on the S-N curve; this can be justified by the rate of relaxation under transverse load, which retains a more significant proportion of the residual stresses. This can be seen when the load approaches the yield strength. The curve obtained shows similar behaviour to that obtained under longitudinal load. The effect of residual stresses gradually drops as the applied load increases. The drop in the endurance limit considered at 106 cycles reaches 110 MPa, based on a linear approximation of the two sets of results.

Effect of load orientation on the fatigue life of welded joint

To compare the effect of load orientation on fatigue life under the influence of residual stresses, we plot in Figure 28 the S-N curves already obtained as well as the reference S-N curve of S355 steel. Initially, we can observe that the effect of the longitudinal load becomes close to the effect of the transverse load at low-stress level. Observing the previous results concerning the evolution of relaxation, it can be confirmed that under low load levels, loading direction has little influence on relaxation rate and on fatigue life.
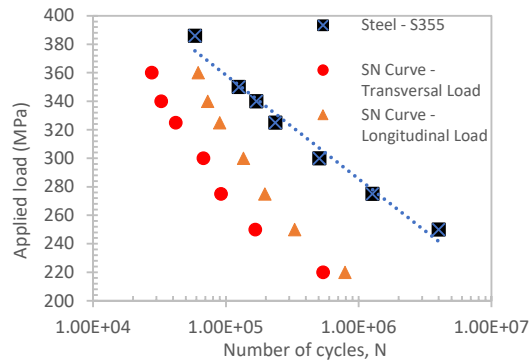

Figure 28. Effect of orientation of the external load on S-N curve

The S-N curve obtained under longitudinal load approaches more quickly the reference fatigue curve of S355 by increasing the applied load. This is due to the strong amount of relaxation of residual stresses under these conditions. By analysing the obtained results, it is noted that the shear strain amplitude on the critical plane remains the same for the two loading cases. However, the normal stress applied to the critical plane under transverse load is more considerable, which explains the difference between the two curves. The fatigue experimental tests obtained for S355 welded plates [59] show similar behaviour to what was obtained by the numerical model. On the welded specimens, and for a fatigue life of 10^6 cycles, the experimental results indicate a stress level slightly lower than 200 MPa. The shape of the obtained curve is also similar to that obtained by the model.

5.0   CONCLUSIONS

The models developed in this paper made it possible to estimate the external load needed to ensure the mechanical strength of structures subjected to monotonic or cyclic load. The results obtained in the first part of this paper reveal the following conclusions:

i.   Under uniaxial load, the longitudinal residual stress field presents the maximum intensity and influences the initiation of relaxation. The level of applied load needed to initiate this relaxation remains stable for the two directions.

ii. Under multiaxial load, the load level required to initiate relaxation depends on the phase difference between the applied loads. In the case where the loads are in opposition, the level of stress needed for relaxation is low.

From these results, the following recommendations can be drawn in the case of moderate load (between 80 and 160 MPa):

i. If the load is uniaxial, consideration of the instability of residual stresses will not be necessary.
ii. If the load is multiaxial, the phase shift must be considered. If the two loads are in phase, it will be possible to consider that the residual stresses are stable but with an error to be taken into account. If the two loads are in opposition (out-of-phase), it will be important to consider the instability of the residual stresses.

In the second part of this paper, we presented a fatigue strength analysis of the welded parts subjected to an external load and internal residual stress. The following conclusions can be drawn:

i. The effect of residual stresses, even after the relaxation process, on the fatigue curve is noticeable; the endurance limit presents a drop varying from 84 to 110 MPa depending on the load orientation.
ii. The effect of the residual stresses varies according to the intensity of the externally applied load. If the applied load is near the yield stress, the effect of the residual stresses is reduced.
iii. The estimation of the fatigue life by considering the superposition between the external load and the state of the residual stresses requires taking into account the tri-axial state of residual stresses and their relaxation. A simple superposition overestimates the effect of residual stresses on the endurance limit.

6.0 ACKNOWLEDGEMENT

7.0 REFERENCES

[1] Y. Zhang, T. Yu, R. Xu, J. Thorborg, W. Liu, et al., "Local residual stresses and microstructure within recrystallizing grains in Iron," *Materials Characterisation*, vol. 191, p. 112113, 2022.

[2] S. Mironov, M. Ozerov, A. Kalinenko, N. Stepanov, O. Plekhov, et al., "On the relationship between microstructure and residual stress in laser-shock-peened Ti-6Al-4V," *Journal of Alloys and Compounds*, vol. 900, p. 163383, 2022.

[3] P.J. Withers, and H.K.D.H. Bhadeshia, "Residual Stress. Part 2 – Nature and Origins," *Materials Science and Technology*, vol. 17, No. 4, pp. 366–375, 2001.

[4] E. Macherauch, "Introduction to residual stress," in *Advances in surface treatments.:Vol. 4 Residual stresses*, A. Niku-Lari, Ed. Oxford: Pergamon Pr, 1987, p. 2.

[5] H. Rashid, G. Hussain, K. Rehman, S. Khan, M. Alkahtani, and M.H Abidi, "Characterisation of residual stresses in an asymmetrical shape produced through incremental forming," *CIRP Journal of Manufacturing Science and Technology*, vol. 31, pp. 478–491, 2020.

[6] C.D.S. Souto, A. Menghini, A. Díaz, J.M. Manso, A.M.P. de Jesus, and C.A. Castiglioni, "Determination of manufacturing residual stresses in cold-formed thin-walled steel profiles." *Thin-Walled Structures*, vol. 180, p. 109945, 2022.

[7] L. Berry, G. Wheatley, W. Ma, R. Masoudi Nejad, and F. Berto, "The influence of milling induced residual stress on fatigue life of aluminum alloys," *Forces in Mechanics*, vol. 7, p. 100096, 2022.

[8] A. Furukawa, K. Kamiya, and M. Hagiwara, "Effect of the residual stress on the fatigue strength of a bolt in bolt/nut assemblies (verification of the hypotheses using an axi-symmetric bolt model)," *Journal of Advanced Mechanical Design, Systems, and Manufacturing*, vol. 6, No. 1, pp. 189–197, 2012.

[9] S. Ao, C. Li, Y. Huang, and Z. Luo, "Determination of residual stress in resistance spot-welded joint by a novel x-ray diffraction," *Measurement*, vol. 161, p. 107892, 2020.

[10] Z. Sun, and X. Yu, "Prediction of welding residual stress and distortion in multi-layer butt-welded 22SiMn2TiB Steel with LTT filling metal," *Journal of Materials Research and Technology*, vol. 18, pp. 3564–3580, 2022.

[11] I.C. Noyan, and J.B. Cohen, *Residual stress: Measurement by diffraction and interpretation*. New York: Springer, 1987.

[12] R. Indukuri, K.V. Pavan, P.R.M. Raju, Ch.S. Rao, and S. Rajesh, "Process parameters optimisation and numerical simulation of laser beam welded butt joints of maraging steel," *International Journal of Automotive and Mechanical Engineering*, vol. 19, No. 2, pp. 9709–9720, 2022.

[13] W. Jiang, Y. Yu, W. Zhang, C. Xiao, and W. Woo, "Residual stress and stress fields change around fatigue crack tip: neutron diffraction measurement and finite element modeling," *International Journal of Pressure Vessels and Piping*, vol. 179, p. 104024, 2020.

[14] Z. Liu, S. Wang, Y. Feng, Y. Peng, J. Gong, and M.A.J. Somers, "Residual stress relaxation in the carburized case of austenitic stainless steel under alternating loading," *International Journal of Fatigue*, vol. 159, p. 106837, 2022.

[15] T. Gray, D. Camilleri, and N. McPherson, *Control of welding distortion in thin-plate fabrication*. Cambridge: Elsevier/Woodhead Publishing, 2014.

[16] V Kumar, N. Ramanaiah, and N. Bhargava Rama Mohan Rao, "Analysis of mechanical, microstructural properties and weld morphology of a-TIG welded AH-36 marine-grade steels with oxide and duplex flux coating," *International Journal of Automotive and Mechanical Engineering*, vol. 18, No. 3, pp. 9101–9112, 2021.

[17] J. Goldak, and A. Chakravarti and M. Bibby, "A new finite element model for welding heat sources," *Metallurgical Transactions B*, vols. 15b, 299, pp. 299–305, 1984.

[18] W.Z. Zhuang, and G.R. Halford, "Investigation of residual stress relaxation under cyclic load," *International Journal of Fatigue*, vol. 23, pp. 31–37, 2001.

[19] S. Schilli, T. Seifert, M. Kreins, and U. Krupp, "Bauschinger effect and latent hardening under cyclic micro-bending of Ni-base alloy 718 single crystals: Part II. Single crystal plasticity modeling with latent kinematic hardening," *Materials Science and Engineering: A*, vol. 830, p. 142030, 2022.

[20] D.C. Drucker, "Background on isotropic criteria," in *Handbook of Materials Behavior Models, Vol. I*, J. Lemaitre, Ed. Academic Press, pp. 129–136, 2001.

[21] A.S. Khan, and S. Huang, *Continuum theory of plasticity*. New York: Wiley, 1995.

[22] J. Guo, K. Xin, and M. He, "comparative study and application of a coupled nonlinear kinematic hardening model for structural metallic material behavior," *Procedia Engineering*, vol. 10, pp. 262–269, 2011.

[23] D.K. Banerjee, W.E. Luecke, M.A. Iadicola, and E. Rust, "Evaluation of methods for determining the yoshida-uemori combined isotropic/kinematic hardening model parameters from tension-compression tests of advanced lightweighting materials." *Materials Today Communications*, vol. 33, p. 104270, 2022.

[24] D. Marquis, "Cyclic plasticity model with nonlinear isotropic and kinematic hardenings, No LIKH model," in *Handbook of Materials Behavior Models Vol. I*, J. Lemaitre, Ed. Academic Press, 2001, pp. 213, 222, 2001.

[25] X. Li, Q. Sun, and X. Zhang, "Identification of combined hardening model parameters by considering pre-tensile stress for 2024-T3 aluminum alloy" *Materials Today Communications*, vol. 26, 2021, p. 102065, 2021.

[26] A.K. Rana, and P.P. Dey, "predicting plastic flow behaviour, failure mechanisms and severe deformation localisation of dual-phase steel using RVE simulation," *International Journal of Automotive and Mechanical Engineering*, vol. 18, no. 1, pp. 8601–8611, 2021.

[27] J. Srnec Novak, F. De Bona, and D. Benasciutti, "An isotropic model for cyclic plasticity calibrated on the whole shape of hardening/softening evolution curve," *Metals*, vol. 9, no. 9, p. 950, 2019.

[28] P.J. Armstrong, and C.O. Frederick, *A mathematical representation of the multiaxial Bauschinger effects*. RD/B/N731, Berkeley Nuclear Laboratories, 1966.

[29] W. Prager, "Recent developments in the mathematical theory of plasticity." *Journal of Applied Physics*, vol. 20, no. 3, pp. 235–241, 1949.

[30] J.L. Chaboche, "A review of some plasticity and viscoplasticity constitutive theories," *International Journal of Plasticity*, vol. 24, no. 10, pp. 1642–1693, 2008.

[31] P. Krolo, D. Grandić, and Z. Smolčić, "Experimental and numerical study of mild steel behaviour under cyclic loading with variable strain ranges," *Advances in Materials Science and Engineering*, vol. 2016, p. 7863010, 2016.

[32] M.N Salleh, M. Ishak, M.H. Aiman, M.M. Quazi, and A.M. Hanafi, "Weld geometry investigation on dissimilar boron steel laser welded for TWB application," *International Journal of Automotive and Mechanical Engineering*, vol. 16, no. 4, pp. 7364–7374, 2019.

[33] B. Schork, U. Zerbst, Y. Kiyak, M. Kaffenberger, M. Madia, and M. Oechsner, "Effect of the parameters of weld toe geometry on the FAT class as obtained by means of fracture mechanics-based simulations," *Welding in the World*, vol. 64, no. 6, pp. 925–936, 2020.

[34] P. Luo, W. Yao, L. Susmel, Y. Wang, and X. Ma, "A survey on multiaxial fatigue damage parameters under non-proportional loadings," *Fatigue & Fracture of Engineering Materials & Structures*, vol. 40, no. 9, pp. 1323–1342, 2017.

[35] P.M. Scott, and T.W. Thorpe, "A critical review of crack tip stress intensity factors for semi-elliptic cracks," *Fatigue & Fracture of Engineering Materials and Structures*, vol. 4, no. 4, pp. 291–309, 1981.

[36] I. Papadopoulos, "A comparative study of multiaxial high-cycle fatigue criteria for metals," *International Journal of Fatigue*, vol. 19, no. 3, pp. 219–235, 1997.

[37] G. Sines, "Behavior of metals under complex static and alternating stresses," In *Metal fatigue,* K.D. Van, I.V. Papadopoulos, Eds. New York: McGraw-Hill, pp. 145–169, 1959.

[38] S.S. Manson, and G.R. Halford, "Multiaxial low-cycle fatigue of type 304 stainless steel," *Journal of Engineering Materials and Technology*, vol. 99, no. 3, pp. 283–285, 1977.

[39] S.Y. Zamrik, M. Mirdamadi, and D.C. Davis. "A proposed model for biaxial fatigue analysis using the triaxiality factor concept," presented at the Advances in Multiaxial Fatigue, San Diego, 1993.

[40] Z. Hashin, "Fatigue failure criteria for combined cyclic stress," *International Journal of Fracture*, vol. 17, no. 2, pp. 101–109, 1981.

[41] N.D. Bibbo, J. Baumgartner, and V. Arora, "Comparative study of critical plane fatigue criteria on multiaxial variable amplitude loaded welded test specimens," *International Journal of Fatigue*, vol. 158, p. 106670, 2022.

[42] A.S Cruces, A. Garcia-Gonzalez, B. Moreno, T. Itoh, and P. Lopez-Crespo, "Critical plane based method for multiaxial fatigue analysis of 316 stainless steel," *Theoretical and Applied Fracture Mechanics*, vol. 118, p. 103273, 2022.

[43] J. Liu, Y. Ran, Y. Wei, and Z. Zhang, "A critical plane-based multiaxial fatigue life prediction method considering the material sensitivity and the shear stress," *International Journal of Pressure Vessels and Piping*, vol. 194, p. 104532, 2021.

[44] D. Shang, G. Sun, J. Deng, and C. Yan, "Multiaxial fatigue damage parameter and life prediction for medium-carbon steel based on the critical plane approach," *International Journal of Fatigue*, vol. 29, no. 12, pp. 2200–2207, 2007.

[45] A. Nourian-Avval, and M.M. Khonsari, "A new model for fatigue life prediction under multiaxial loadings based on energy dissipation," *International Journal of Fatigue*, vol. 151, p. 106255, 2021.

[46] J. Li, X. Wang, R. Li, and Y. Qiu, "Multiaxial fatigue life prediction for metals by means of an improved strain energy density-based critical plane criterion," *European Journal of Mechanics - A/Solids*, vol. 90, p. 104353, 2021.

[47] S.A.N. Mohamed, S. Abdullah, A. Arifin, A.K. Ariffin, and M.M. Padzi, "Characterisation of the biaxial fatigue behaviour on medium carbon steel using the strain-life approach," *International Journal of Automotive and Mechanical Engineering*, vol. 13, no. 1, pp. 3262–3277, 2016.

[48] R. Wang, C. Lu, K.A. Tieu, and A.A. Gazder, "Slip system activity and lattice rotation in polycrystalline copper during uniaxial tension," *Journal of Materials Research and Technology*, vol. 18, pp. 508–519, 2022.

[49] Z. Zhao, and S. To, "An investigation of resolved shear stress on activation of slip systems during ultraprecision rotary cutting of local anisotropic Ti-6Al-4V alloy: Models and experiments," *International Journal of Machine Tools and Manufacture*, vol. 134, pp. 69–78, 2018.

[50] M.D. Sangid, H.J. Maier, and H. Sehitoglu, "A physically based fatigue model for prediction of crack initiation from persistent slip bands in polycrystals," *Acta Materialia*, vol. 59, No. 1, pp. 328–341, 2011.

[51] C. Bathias, and A. Pineau, "Introduction to fatigue: Fundamentals and methodology," in *Fatigue of materials and structures: fundamentals*, C. Bathias, and A. Pineau, Eds., London: John Wiley, 2010, pp. 11–12.

[52]   L. Fourel, J.-P. Noyel, E. Bossy, X. Kleber, P. Sainsot, and F. Ville, "Towards a grain-scale modeling of crack initiation in rolling contact fatigue - Part 2: Persistent slip band modeling," *Tribology International*, vol. 163, p. 107173, 2021.

[53]   R.P. Kaufman, and T. Topper, "The influence of static mean stresses applied normal to the maximum shear planes in multiaxial fatigue," in *European Structural Integrity Society*, vol. 31, pp. 123–143, 2003.

[54]   W.N. Findley, "A theory for the effect of mean stress on fatigue of metals under combined torsion and axial load or bending," *Journal of Engineering for Industry*, vol. 81, no. 4, pp. 301–305, 1959.

[55]   A. Karolczuk, and E. Macha, "Fatigue fracture planes and the critical plane orientations in multiaxial fatigue failure criteria," presented at the Crack Paths (CP 2006), Parma, Italy, 2006.

[56]   A. Fatemi, and DF Socie, "A critical plane approach to multiaxial fatigue damage including out-of-phase loading," *Fatigue & Fracture of Engineering Materials and Structures*, vol. 11, no. 3, pp. 149–165, 1988.

[57]   A. Karolczuk, and E. Macha, "A review of critical plane orientations in multiaxial fatigue failure criteria of metallic materials," *International Journal of Fracture*, vol. 134, nos. 3–4, pp. 267–304, 2005.

[58]   A. Cruces, P. Lopez-Crespo, B. Moreno, and F. Antunes, "Multiaxial fatigue life prediction on S355 structural and offshore steel using the SKS critical plane model," *Metals*, vol. 8, no. 12, p. 1060, 2018.

[59]   P.M.V. Monteiro, and RF da S. Santos, "Fatigue resistance of butt welds of structural steels in wind towers," M.S. thesis, University of Porto, Portugal, 2019.